

# First-principles study of the lattice and electronic structures of $\text{TbMn}_2\text{O}_5$

Chenjie Wang, Guang-Can Guo, and Lixin He \*

*Key Laboratory of Quantum Information, University of Science and Technology of China, Hefei, 230026, People's Republic of China*

(Dated: February 2, 2008)

The structural, electronic and lattice dielectric properties of multiferroic  $\text{TbMn}_2\text{O}_5$  are investigated using density functional theory within the generalized gradient approximation (GGA). We use collinear spin approximations and ignore the spin-orbit coupling. The calculated structural parameters are in excellent agreement with the experiments. We confirm that the ground state structure of  $\text{TbMn}_2\text{O}_5$  is of space group  $Pb2_1m$ , allowing polarizations along the  $b$ -axis. The spontaneous electric polarization is calculated to be  $1187 \text{ nC}\cdot\text{cm}^{-2}$ . The calculated zone-center optical phonons frequencies and the oscillator strengths of IR phonons agree very well with the experimental values. We then derive an effective Hamiltonian to explain the magnetically-induced ferroelectricity in this compound. Our results strongly suggest that the ferroelectricity in  $\text{TbMn}_2\text{O}_5$  is driven by the magnetic ordering that breaks the inversion symmetry, without invoking the spin-orbit coupling.

PACS numbers: 75.25.+z, 77.80.-e, 63.20.-e

## I. INTRODUCTION

Recently, a large class of manganese oxides ( $\text{RMnO}_3$ ,<sup>1,2</sup> and  $\text{RMn}_2\text{O}_5$ ,<sup>3,4,5</sup> with  $\text{R}=\text{Y}$ ,  $\text{Tb}$ ,  $\text{Dy}$ , etc.) has been discovered to be multiferroic, with strong magnetoelectric (ME) coupling. The ME coupling leads to various novel physical effects, such as the “colossal magnetodielectric” (CMD) effects and magneto-spin-flop effects.<sup>1,2,6</sup> For example, in  $\text{TbMn}_2\text{O}_5$ ,<sup>3,7</sup> the ME coupling is so strong, that the electric polarization can be reversed by applying a magnetic field.<sup>3</sup> The remarkable ME effects revealed in these materials have attracted great attention<sup>1,2,3,4,5,7,8,9,10,11,12</sup> because of the fascinating physics and their potential applications in novel multifunctional ME devices.

The crystal structure of  $\text{TbMn}_2\text{O}_5$  is orthorhombic, with four chemical formula units per primitive cell (32 atoms in total), containing  $\text{Mn}^{4+}\text{O}_6$  octahedra and  $\text{Mn}^{3+}\text{O}_5$  pyramids, as shown in Fig.1.  $\text{TbMn}_2\text{O}_5$  shows several magnetic phase transitions accompanied with the appearance of electric polarizations and dielectric anomalies, when cooling down from the room temperature.<sup>3,4,5</sup> Starting from an incommensurate antimagnetic (ICM) ordering at  $T_N = 43\text{K}$  with a propagation vector  $\mathbf{k}$  ( $\sim 0.50, 0, 0.30$ ), the structure locks into commensurate antimagnetic (CM) state at  $T_{CM} = 33\text{K}$  with  $\mathbf{k}=(0.5, 0, 0.25)$ , during which spontaneous polarization arises at  $T_{FE} = 38\text{K}$ .<sup>3,4</sup> When the temperature lowers to  $T_{ICM} = 24\text{K}$ , magnetic order becomes ICM again, with a sudden decrease of polarization and a jump of the  $\mathbf{k}$  vector to  $(0.48, 0, 0.32)$ . The spontaneous polarization increase again, when continuing to cool to about  $10\text{K}$ .<sup>3</sup> During the magnetic phase transitions, a peak at  $T_{FE}$  and a step at  $T_{ICM}$  of the dielectric constant was observed,<sup>3,4</sup> indicating strong ME coupling in this compound. It was

demonstrated the electric polarization can be reversed by applying magnetic field.<sup>3</sup>

Experimental data show that the structure of  $\text{TbMn}_2\text{O}_5$  has space group  $Pbam$ ,<sup>13</sup> which includes spatial inversion ( $R^{-1}$ ) symmetry. It is therefore puzzling that the material can develop spontaneous electric polarizations. It has been suspected<sup>4,9</sup> that the actual symmetry group of  $\text{TbMn}_2\text{O}_5$  is  $Pb2_1m$ , allowing polarization along the  $b$  axis. Indeed, there are several experiments supporting this hypothesis.<sup>4,5,10</sup> For example, some Raman modes were found to be IR active in  $\text{TbMn}_2\text{O}_5$ ,<sup>10</sup> and the anomalies of atomic displacement parameters (ADP) have been observed.<sup>4</sup> Nevertheless, no *direct* evidence of the lower symmetry has yet been found.<sup>4,5</sup>

Theoretically, the microscopic origin of the strong ME coupling and the electric polarization is still under intensive debates.<sup>4,7,11,12</sup> The ME coupling could originate either from the symmetric superexchange interactions, or from the antisymmetric exchange interactions.<sup>8</sup> The antisymmetric exchange comes from the spin-orbit coupling, and the noncollinearity of the spin structure is an essential ingredient for this mechanism.<sup>8,11,12,14</sup> However it was shown in Ref. 4 that the largest electric polarization in  $\text{TbMn}_2\text{O}_5$  is associated with the CM state that is almost collinear.<sup>15</sup> In our recent work,<sup>16</sup> we determined the ground-state structure of  $\text{TbMn}_2\text{O}_5$  using the first-principles methods. The results show that the ground-state structure is indeed of polar space group  $Pb2_1m$  and the electric polarization equals  $1187 \text{ nC}\cdot\text{cm}^{-2}$ . In the calculations, we use collinear spin approximation and ignore the spin-orbit interaction, suggesting that ME coupling in  $\text{TbMn}_2\text{O}_5$  is due to the symmetric superexchange interactions.

The aim of the present work to examine rigorously the ground state structural, electronic and lattice dielectric properties of  $\text{TbMn}_2\text{O}_5$  using first-principles calculations to provide solid ground for further investigations. The rest of paper is organized as follows. After a brief discussion of the first-principles methods and the approxi-

\*corresponding author, Email address: helx@ustc.edu.cn

TABLE I: The calculated lattice constants compared with experimental data. *FM* and *L* are the structures of spin configurations *a* and *g* in Fig. 2, respectively.

lattice const. (Å).	<i>FM</i>	<i>L</i>	Exp. <sup>13</sup>
a	7.3170	7.3014	7.3251
b	8.5269	8.5393	8.5168
c	5.6611	5.6056	5.6750

mations used in the calculations in Sec. II, we provide a detailed analysis of the ground-state structural and electronic properties in Sec. III, IV. In Sec. V, we calculate all zone center optical phonon frequencies and the oscillator strengths of IR modes. The results are in excellent agreement with the known experimental IR and Raman spectra. In Sec. VI, we calculate electric polarization in  $\text{TbMn}_2\text{O}_5$ . We then derive an effective Hamiltonian to explain the microscopic mechanisms of the ferroelectricity and the giant magnetoelectric coupling. We conclude in Sec. VII.

## II. METHODOLOGY

Our calculations are based on the standard density-functional (DFT) theory with spin-polarized generalized gradient approximation (GGA). We adopt Perdew-Burke-Ernzerhof functional<sup>17</sup> implemented in the Vienna *ab initio* Simulations Package (VASP).<sup>18,19</sup> A plane-wave basis and projector augmented-wave (PAW) pseudopotentials<sup>20</sup> are used, with Mn  $3p3d4s$ , and Tb  $5p5d6s$  electrons treated self-consistently. A 500 eV plane-wave cutoff results in good convergence of the total energies. We relax the structure until the changes of total energy in the self-consistent calculations are less than  $10^{-7}$  eV, and the remaining forces are less than 1 meV/Å. Experimentally,  $\text{TbMn}_2\text{O}_5$  is found to be incommensurate anti-ferromagnetic (AFM) below 24 K, with the propagation vector  $\mathbf{k} \approx (0.48, 0, 0.32)$ . To accommodate the magnetic structure, one needs a huge supercell, which is computationally prohibitive. Instead, we use a  $2 \times 1 \times 1$  supercell, equivalent to approximating the propagation vector  $\mathbf{k} = (0.5, 0, 0)$ . The validity of this approximation has been justified in our previous work.<sup>16</sup> For the supercell we used, a  $1 \times 2 \times 4$  Monkhorst-Pack  $k$ -points mesh converges very well the results.

It was demonstrated in Ref. 4 that the largest electric polarization is associated with a commensurate magnetic (CM) state that is almost collinear.<sup>15</sup> Therefore, in the calculations, we use the collinear spin approximation and ignore the spin-orbit coupling. Our results agree very well with the known experiments, indicating that these approximations capture the essential physics in  $\text{TbMn}_2\text{O}_5$ .

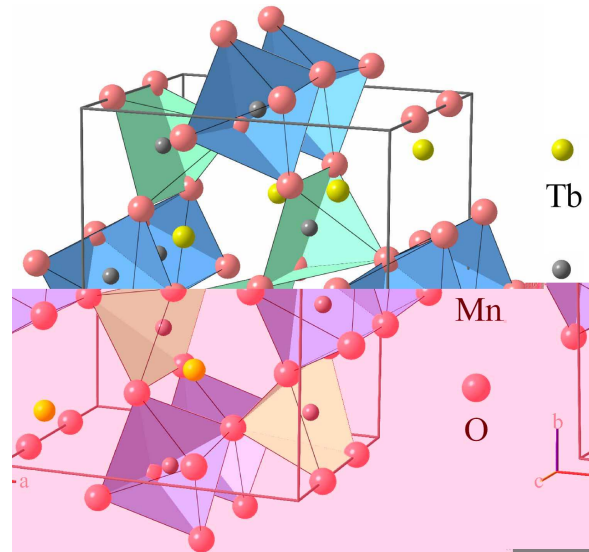


FIG. 1: (Color online) Structure of  $\text{TbMn}_2\text{O}_5$  unit cell, showing  $\text{Mn}^{4+}\text{O}_6$  Octahedra and  $\text{Mn}^{3+}\text{O}_5$  pyramids.

## III. GROUND-STATE STRUCTURE

We start the structural relaxation from the experimental structural parameters.<sup>13</sup> To determine the ground state structure, we tried various spin configurations (SCs). Eight selected SCs, four ferromagnetic/ferrimagnetic (FM) and four antiferromagnetic (AFM), are shown in Fig.2. Here, we consider only the spins of  $\text{Mn}^{3+}$  and  $\text{Mn}^{4+}$  ions. The total energy of each SCs is calculated with full relaxations of the (electronic and lattice) structures. The stablest SC, i.e., the SC of lowest total energy, labeled as *g* in Fig.2 is AFM and is identical to the spin structure proposed in Ref.4. SC *g* has an energetically degenerate SC,<sup>16</sup> labeled as *g'* in Fig. 3. In both SCs *g* and *g'*,  $\text{Mn}^{4+}$  form an AFM square lattice in the *ab* plane, whereas  $\text{Mn}^{3+}$  couples to  $\text{Mn}^{4+}$  either antiferromagnetically via  $J_4$  along *a* axis or with alternating sign via  $J_3$  along the *b* axis.  $\text{Mn}^{3+}$  ions in two connected pyramids also couple antiferromagnetically through  $J_5$ . Here, we adopt the notations  $J_3$ ,  $J_4$  and  $J_5$  from Ref. 4, and define the  $J_3$  to be the  $\text{Mn}^{4+}$ - $\text{Mn}^{3+}$  superexchange interaction through pyramidal base corners, and  $J_4$  the superexchange interaction through the pyramidal apex, as indicated in Fig. 3. We label the two different  $\text{Mn}^{4+}$  chains along the *a* axis I, II, respectively, also following Ref. 4. The magnetic structure of *g'* can be obtained from *g* by shifting chain II to the right (or to the left) by one unit cell along the *a* axis.<sup>4</sup> The exchange integrals  $J_3$ ,  $J_4$ ,  $J_5$ , were fitted via a Heisenberg model assuming nearest neighbor (NN) coupling. We find that all the exchange energies are of AFM type, i.e., negative and  $|J_4|, |J_5| \gg |J_3|$ . Therefore, the spins must couple via  $J_4$  and  $J_5$  anti-ferromagnetically in the stable magnetic structures. More details about the spin structure is given in Appendix A.

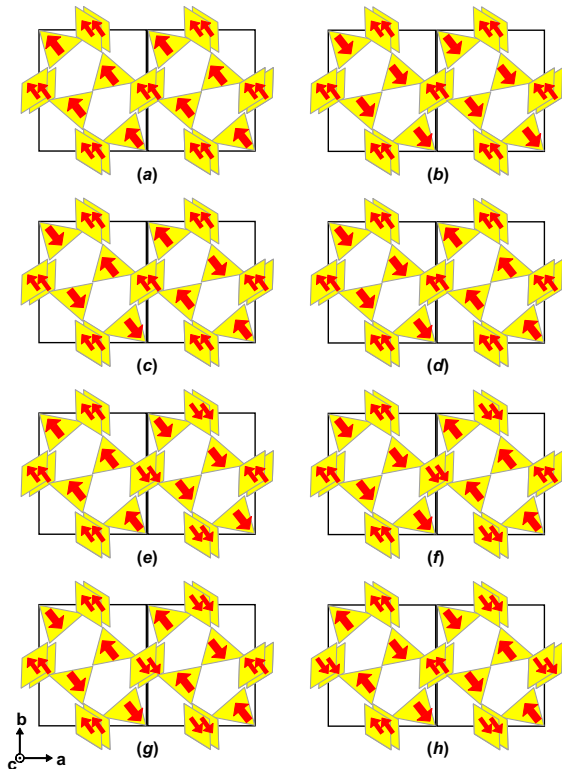


FIG. 2: (Color online) Spin configurations of  $\text{Mn}^{3+}$ ,  $\text{Mn}^{4+}$  ions in the  $ab$  plane.

The lattice structure relaxed from SC  $g$  lead to structure  $L$  in Ref. 16, whereas SC  $g'$  gives the structure  $R$ . The calculated lattice constants<sup>16</sup> of the ground state structure  $L$  (and  $R$ ) are listed in Table I, and are in very good agreement with the experiments.<sup>13</sup> The errors of the lattice constants are about 1%, typical errors

for GGA. The lattice constants calculated for the full FM configuration (SC  $a$ ), are also listed in Table I, which are somewhat different from those of structure  $L$ . The calculated Wyckoff positions (WPs) for the structure  $L$  are given in Table II, comparing with the experimental data,<sup>13</sup> whereas the structure  $R$  is a mirror image of  $L$  about the  $ac$ -plane. The calculated WPs positions are extremely close to what was obtained experimentally. However, the WPs of structure  $L$  split by small amount from the WPs of the ( $Pbam$ ) experimental structure, and lower the structural symmetry to the long searched  $Pb2_1m$  polar group.<sup>9</sup> The relationships between the WPs of  $\text{TbMn}_2\text{O}_5$  under  $Pbam$  symmetry and under the  $Pb2_1m$  symmetry are given in Table III. For example, under the  $Pbam$  symmetry,  $\text{Mn}^{3+}$  has one WP (notation h), with four equivalent sites. It splits into two WPs b(1) and b(2), each having two equivalent sites, when the symmetry lowers to  $Pb2_1m$ .

We artificially construct a high symmetry structure  $H$  by symmetrizing structure  $L$  and  $R$  according to the  $Pbam$  symmetry.<sup>16</sup> The WPs of  $H$  together with the atomic displacements from  $H$  to  $L$  are also given in Table II, where  $\delta a$ ,  $\delta b$  and  $\delta c$  denote the atomic displacements from the high symmetry positions along the  $a$ ,  $b$  and  $c$  axes respectively. The displacements along the  $a$  and  $c$  axes are of mirror symmetry, whereas the displacements along the  $b$  axis are not. As seen in Table II, all cations move up and anions (except  $\text{O}_1$ ) move down from the positions of high symmetry structure  $H$ , resulting in polarization. However, all the atomic displacements are extremely small, usually are of the order of  $\sim 10^{-4}$  of the lattice constants. Therefore the low symmetry structure can not be directly determined experimentally, and only the anomalies of the atomic displacement parameters (ADPs) were observed.<sup>4</sup> The largest atomic displacements come from  $\text{Mn}^{3+}$ , and  $\text{O}_3$ ,  $\delta y \sim 10^{-3}$  of the lattice constants, in agreement with the ADP results of Ref.4.

#### IV. ELECTRONIC STRUCTURE

Figure 4 depicts the calculated the total densities of states (DOS) of structure  $L$ . The DOS of spin-up and spin-down electrons are identical as expected for an AFM state. From the results, the band gap is estimated to be  $\sim 0.4$  eV, confirming the experimental fact that  $\text{TbMn}_2\text{O}_5$  is an insulator. However, it is well known that GGA greatly underestimates the band gap, especially for the  $3d$  compounds, therefore the real band gap might be much larger. We further calculated the site-projected partial DOS (PDOS) for Tb, Mn  $d$  electrons and O  $p$  electrons in the energy range of -2.5 to 2.5 eV around the Fermi level, shown in Fig.5. In structure  $L$ , the Tb,  $\text{Mn}^{3+}$ ,  $\text{O}_2$ ,  $\text{O}_3$  and  $\text{O}_4$  each has two non-equivalent sites, and the PDOS are shown separately. The PDOS for other

electrons are quite small in the selected energy range and therefore are not shown. We see the DOS near the Fermi level is mainly from Mn  $3d$  and O  $2p$  orbitals.

The local magnetic moments are estimated for  $\text{Mn}^{3+}$  to be  $\sim 2.37 \mu_B$ , and for  $\text{Mn}^{4+}$  to be  $\sim 1.64 \mu_B$ , in a good agreement with the refined magnetic moments.<sup>4</sup> The ionic radii of 0.60 Å and 0.66 Å are used for  $\text{Mn}^{4+}$  and  $\text{Mn}^{3+}$  respectively taken from the periodic table. The local magnetic moments of  $\text{Mn}^{3+}$ , and  $\text{Mn}^{4+}$  at different WPs are slightly different. O ions also have small induced magnetic moments, due to their hybridization with Mn ions. The calculated local moments of Tb are extremely small, whereas  $1.6 \mu_B$  is assumed in order to obtain a perfect fit of the neutron diffraction data in Ref. 4. The difference might come from that the  $f$  electrons are not included as valence electrons in the Tb pseudopotential.

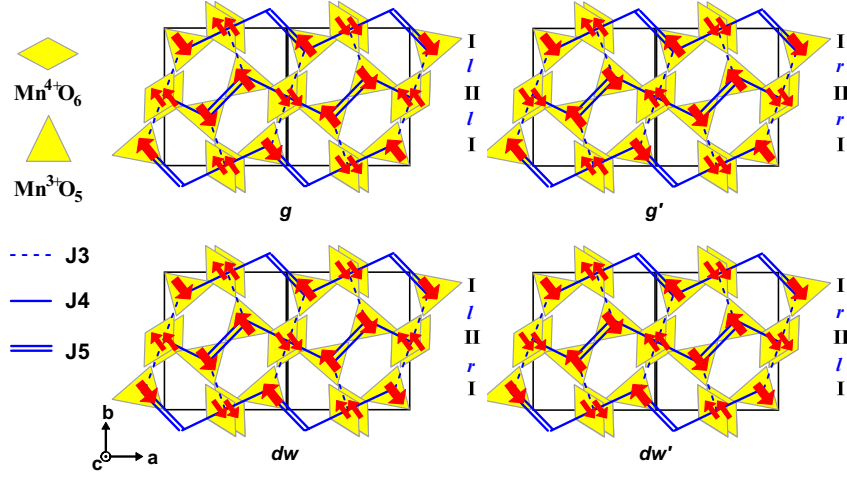


FIG. 3: (Color online) Spin configurations with different combinations of chains I and II.  $g$  and  $g'$  are the ground state spin configurations for structure  $L$  and  $R$  respectively, whereas  $dw$  and  $dw'$  are the domain walls between structure  $L$  and  $R$ .

TABLE II: Comparison of the calculated and measured atom positions of  $\text{TbMn}_2\text{O}_5$ .  $L$  and  $H$  are the ground state structure and the high-symmetry structure respectively.  $|\delta a|$ ,  $|\delta b|$ , and  $|\delta c|$  denote the atomic displacements from  $H$  to  $L$ . The experimental values are taken from Ref. 13.

atom	$L$ ( $Pb2_1m$ )			$H$ ( $Pbam$ )			$H \rightarrow L (10^{-4})$			Exp. ( $Pbam$ )		
	a	b	c	a	b	c	$ \delta a $	$ \delta b $	$ \delta c $	a	b	c
$\text{Tb}_1^{3+}$	0.1410	0.1733	0	0.1407	0.1732	0	3.0	1.5	0	0.1399	0.1726	0
$\text{Tb}_2^{3+}$	0.6404	0.3270	0				3.0	1.5	0			
$\text{Mn}^{4+}$	0.0001	0.5003	0.2558	0	0.5	0.2558	0.8	2.9	0	0	0.5	0.2618
$\text{Mn}_1^{3+}$	0.4012	0.3558	0.5	0.4014	0.3551	0.5	2.2	6.6	0	0.4120	0.3510	0.5
$\text{Mn}_2^{3+}$	0.9016	0.1456	0.5				2.2	6.6	0			
O1	0.0008	0.0002	0.2709	0	0	0.2709	8.2	2.3	0	0	0	0.2710
O2 <sub>1</sub>	0.1646	0.4480	0	0.1647	0.4481	0	1.2	1.2	0	0.1617	0.4463	0
O2 <sub>2</sub>	0.6648	0.0517	0				1.2	1.2	0			
O3 <sub>1</sub>	0.1560	0.4329	0.5	0.1565	0.4337	0.5	5.3	7.8	0	0.1528	0.4324	0.5
O3 <sub>2</sub>	0.6571	0.0655	0.5				5.3	7.8	0			
O4 <sub>1</sub>	0.3977	0.2077	0.2438	0.3968	0.2079	0.2430	8.8	2.2	8.5	0.3973	0.2062	0.2483
O4 <sub>2</sub>	0.8959	0.2919	0.7579				8.8	2.2	8.5			

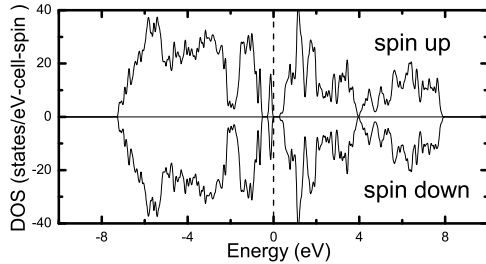


FIG. 4: The total density of states (DOS) of  $\text{TbMn}_2\text{O}_5$  for spin-up and spin-down respectively, calculated under structure  $L$ . The dashed line represents the Fermi level.

TABLE III: The Wyckoff positions (WPs) for each inequivalent atom in  $\text{TbMn}_2\text{O}_5$  under the space group  $Pbam$  and its subgroup  $Pb2_1m$ .

Atoms	WP( $Pbam$ )	WP( $Pb2_1m$ )
$\text{Tb}^{3+}$	4g	2a, 2a
$\text{Mn}^{4+}$	4f	4c
$\text{Mn}^{3+}$	4h	2b, 2b
O1	4e	4c
O2	4g	2a, 2a
O3	4h	2b, 2b
O4	8i	4c, 4c

We also calculated the DOS and PDOS of structure  $H$  and find no obvious differences from structure  $L$ , suggesting that the effects of the lattice structure distortion and

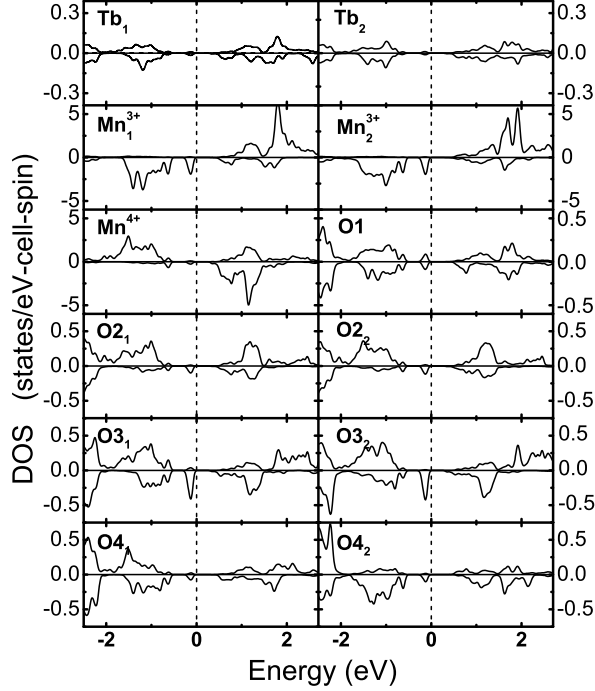


FIG. 5: Site-projected partial density of states (PDOS) of Mn and Tb  $d$  electrons, and O  $p$  electrons for  $\text{TbMn}_2\text{O}_5$ . The upper panel and lower panel show the PDOS for spin up and spin down respectively. The PDOS of other states are relatively small in the selected energy range, and therefore not shown. The dashed lines represent the Fermi level.

TABLE IV: The relationships of irreducible representations between space group  $Pbam$  and its subgroup  $Pb2_1m$ .

$Pb2_1m$		$Pbam$	
irreps	Character	irreps	Character
$A_1$	IR and Raman	$A_g$	Raman
$B_1$	IR and Raman	$B_{2u}$	IR
$B_2$	IR and Raman	$B_{3g}$	Raman
$A_2$	Raman	$B_{1u}$	IR
		$B_{1g}$	Raman
		$B_{3u}$	IR
		$B_{2g}$	Raman
		$A_u$	Silent

the symmetry lowering in structure  $L$  to the electronic structure are small.

## V. LATTICE DYNAMIC PROPERTIES

The symmetry lowering and ferroelectricity in the traditional ferroelectrics, such as  $\text{BaTiO}_3$ ,  $\text{PbTiO}_3$ , etc. are driven by the condensation of zone center soft phonons.<sup>21</sup> In  $\text{TbMn}_2\text{O}_5$ , the low symmetry ( $Pb2_1m$ ) structure was

not observed *directly* in the experiments. However, a strong evidence that suggests the symmetry lowering is that one of the Raman-active phonons become also IR-active at low temperature,<sup>10</sup> which is forbidden by the higher  $Pbam$  symmetry. To elucidate the origin of the symmetry lowering, we calculate the frequencies of all zone center phonons, using frozen phonon method, to exam if any soft modes exist in  $\text{TbMn}_2\text{O}_5$  and the symmetry properties of all phonons. Furthermore, the validity of our theories can be examined by comparing the calculated phonons with experiments.

### A. symmetry analysis

We first carry out symmetry analyses and decompose the symmetry-adapted modes into irreducible representations. The Hamiltonian remains invariant under a lattice translation of the 32-atom primitive cell combined with spin reversal. Therefore the force-constant matrix has the translational symmetry of the 32-atom primitive cell.<sup>22</sup> We then perform the symmetry analyses on the 32-atom primitive cell (instead of the 64-atom AFM cell used in the calculations), using the SMODES symmetry-analysis software package.<sup>23</sup>

For the high symmetry structure ( $Pbam$ ), all the 96 modes, including 3 acoustic modes, are decomposed into 8 irreducible representations (irreps):

$$\Gamma(Pbam) = 9B_{1u} \oplus 15B_{2u} \oplus 15B_{3u} \oplus 13A_g \oplus 13B_{1g} \oplus 11B_{2g} \oplus 11B_{3g} \oplus 9A_u. \quad (1)$$

Among them  $B_{3u}$ ,  $B_{2u}$  and  $B_{1u}$  modes are IR active, polarized along the  $a$ ,  $b$  and  $c$  axis, respectively, whereas  $B_{1g}$ ,  $B_{2g}$ ,  $B_{3g}$  and  $A_g$  modes are Raman active and  $A_u$  modes are silent. All these irreps are one dimensional, i.e., no degenerate phonons. The three acoustic modes are each in one of the three IR-active representations. As we see, the Raman- and IR-active modes do not couple under the  $Pbam$  symmetry.

For the crystal structure processes a  $Pb2_1m$  symmetry, the 96 phonons can be decomposed into 4 irreps:

$$\Gamma(Pb2_1m) = 28A_1 \oplus 20B_1 \oplus 28B_2 \oplus 20A_2. \quad (2)$$

We found all modes are Raman active, among them  $A_1$ ,  $B_1$  and  $B_2$  are also IR active, which are polarized along the  $b$ ,  $c$ , and  $a$  axis respectively.<sup>10</sup> The relationships between the irreps of  $Pbam$  symmetry and its subgroup  $Pb2_1m$  symmetry are given in Table IV, together with the symmetry character for each irrep. The  $A_1$  modes are coupled from the  $A_g$  and  $B_{2u}$  modes and the  $A_2$  modes are composed of the  $B_{2g}$  and  $A_u$  modes. The  $B_1$  modes are the coupled  $B_{3g}$  and  $B_{1u}$  modes whereas the  $B_2$  modes are the coupled  $B_{1g}$  and  $B_{3u}$  modes.

TABLE V: Calculated phonon frequencies  $\omega$ , effective charges  $Z_\lambda^*$  and oscillator strength  $S_\lambda$  of  $A_1$  modes, classified according to their major symmetry characters and compared with the experimental data. The IR-active phonons are extracted from Ref. 10 at 7K and Raman-active phonons are extracted from Ref. 24.

$B_{2u}(\text{IR}, b\text{-polarized})$							$A_g(\text{Raman})$				
$\omega$		$Z_\lambda^*$		$S_\lambda$		Raman%	$\omega$		$Z_\lambda^*$		IR%
GGA	Exp.	GGA	Exp.	GGA	Exp.		GGA	Exp.	GGA	GGA	
100.7	97.2	0.09	0.17	0.11	0.42	0.08	110.1		0.020	0.005	0.02
158.0	168.9	0.28	0.31	0.44	0.46	0.12	136.9		-0.003	$\sim 0$	0.17
162.8	171.9	0.31	0.25	0.49	0.30	0.04	221.6	215	0.058	0.009	0.94
224.8	222.2	0.30	0.20	0.24	0.11	1.85	235.1	221	0.066	0.011	1.38
267.3	256.8	0.25	0.28	0.12	0.17	0.36	312.5	334	0.125	0.022	0.97
316.7	333.4	0.78	0.37	0.82	0.17	1.02	340.2	350	0.094	0.011	2.96
351.3	386	0.28	0.15	0.09	0.02	2.94	405.6	412	-0.028	$\sim 0$	0.24
412.5	422.3	0.39	0.60	0.13	0.28	0.23	445.1		0.423	0.126	2.24
439.5	453.2	2.58	2.25	4.81	3.43	2.65	489.2	500	0.151	0.013	6.51
471.0	481.8	1.40	2.18	1.23	2.86	5.89	529.2	537	-0.104	0.005	6.16
533.5	538.2	0.52	0.72	0.27	0.25	5.95	612.0	621	-0.002	$\sim 0$	3.28
549.3	567.3	0.50	1.09	0.12	0.52	1.33	613.5	631	0.030	$\sim 0$	9.59
625.0	636.6	1.01	0.88	0.36	0.27	11.20	673.6	693 <sup>a</sup>	-0.107	0.004	8.04
667.2	688.3	0.17	0.10	0.01	0.003	8.83					

<sup>a</sup>IR-active and 703  $\text{cm}^{-1}$  measured by Aguilar<sup>10</sup>

TABLE VI: Calculated phonon frequencies  $\omega$ , effective charges  $Z_\lambda^*$  and oscillator strength  $S_\lambda$  of  $B_2$  modes, classified according to their major symmetry characters and compared with the experimental data. The IR-active phonons are extracted from Ref. 10 at 7K and Raman-active phonons extracted from Ref. 24.

$B_{3u}(\text{IR}, a\text{-polarized})$							$B_{1g}(\text{Raman})$				
$\omega$		$Z_\lambda^*$		$S_\lambda$		Raman%	$\omega$		$Z_\lambda^*$		IR%
GGA	Exp.	GGA	Exp.	GGA	Exp.		GGA	Exp.	GGA	GGA	
111.8	111.9	0.02	0.23	0.004	0.59	0.02	148.2	148	0.007	$\sim 0$	0.54
152.2	157.5	0.17	0.37	0.18	0.81	0.50	172.9	172	0.006	$\sim 0$	0.13
159.8	164.2	0.76	0.57	3.11	1.68	0.12	222.1	208	0.054	0.008	10.5
217.4	218.5	0.05	0.32	0.01	0.30	10.99	243.0	237	0.067	0.011	0.97
264.5	254.8	0.30	0.94	0.18	1.88	0.62	300.7	326	0.007	$\sim 0$	0.18
317.0	333.1	0.03	0.27	0.002	0.09	0.15	373.0		0.048	0.002	9.50
353.1	364.9	1.04	1.39	1.21	2.02	1.25	410.4	416	0.019	$\sim 0$	0.31
379.1	397.6	0.56	0.66	0.30	0.38	8.44	470.0	485	0.360	0.081	36.8
465.2		0.21		0.03		1.20	518.3		0.115	0.007	2.82
474.4	494.8	0.24	0.89	0.03	0.45	37.76	545.8	538	0.054	0.001	0.58
509.2		1.18		0.75		0.59	587.1		0.178	0.013	1.91
595.4	613.5	0.90	1.38	0.32	0.71	1.28	643.8	673	0.445	0.067	5.35
617.1	627.5	1.23	0.81	0.55	0.23	4.57	678.7	697	0.027	$\sim 0$	10.0
672.7	704.2	0.33	0.42	0.03	0.05	12.12					

## B. Zone Center Optical Phonons

The zone-center phonons frequencies are calculated via a frozen phonon technique.<sup>22</sup> For each irrep  $\Gamma$  in Eq. (1), (2), we construct an  $N_\Gamma \times N_\Gamma$  dynamical matrix from a series of frozen-phonon calculations in which the structure is distorted according to each of the  $N_\Gamma$  symmetry modes in this irrep. For example,  $N_\Gamma=28$  for the  $A_1$  modes in Eq. (2). All calculations were performed in the 64-atom AFM cell respect to the correct AFM reference ground state. After calculating the residual Hellmann-Feynman forces we displace the ions according to the symmetry

coordinate for each mode by 0.1% of lattice constant and calculate the forces  $F_i^\alpha$  on ion  $i$  in Cartesian direction  $\alpha$  due to displacements  $u_j^\beta$  of ion  $j$  in direction  $\beta$ . The force constant matrix

$$\Phi_{ij}^{\alpha\beta} = -\frac{\partial F_i^\alpha}{\partial u_j^\beta}, \quad (3)$$

is then obtained by finite differences to the residual forces in the equilibrium structure to eliminate the numerical errors due to the residual forces. The normal modes  $\mathbf{u}_\lambda$  and their frequencies  $\omega_\lambda$  are then obtained through solu-

tion of the eigenvalue equation

$$\Phi \cdot \mathbf{u}_\lambda = \omega_\lambda^2 \mathbf{M} \cdot \mathbf{u}_\lambda. \quad (4)$$

Here  $M_{ij}^{\alpha\beta} = (m_i/m_0) \delta_{ij} \delta_{\alpha\beta}$  is the dimensionless diagonal mass matrix, where  $m_i$  is the mass of atom  $i$  and  $m_0$  is a reference mass chosen here to be 1 amu, and the eigenvectors are normalized according to  $\mathbf{u}_\mu \cdot \mathbf{M} \cdot \mathbf{u}_\nu = \delta_{\mu\nu}$ .

The phonon frequencies calculated from high structure  $H$  are extremely close to those calculated from low symmetry structure  $L$ . No soft mode is found in both high and low symmetry structures, excluding the possibility of ferroelectricity driven by the soft modes. We therefore show only the phonon frequencies for the ground state structure  $L$  only. The calculated  $A_1$ ,  $B_2$ ,  $B_1$  phonon frequencies are given in Table V, Table VI, and Table VII respectively, whereas the  $A_2$  phonons are given in Table VIII. To make a good contact with experiments, we divide the phonons of each irrep into two presentations according to their major symmetry characters (see Table IV). We found that for most of the modes the coupling between the major and minor characters (IR and Raman or Raman and silent) are extremely small, and such classification is unambiguous. All calculated phonon frequencies are in excellent agreement with the experiments especially for the low-frequency phonons. The errors are less than 5%.

In order to check the influences on phonons from different magnetic orderings and magnetic-ordering-induced lattice modulations, we also calculated the phonon frequencies for the FM structure, we find the differences are also small.

In the following sections, we compare the calculated IR and Raman spectra with the experiments in details.

### 1. IR spectra and dielectric properties

Aguilar *et al.* measured the frequencies of IR-active phonon polarized along the  $b$  and  $a$  axes.<sup>10</sup> These phonon modes are compared with the calculated modes in Table V and Table VI, respectively.

For the IR phonons, we can further calculate their contribution to the dielectric constant. The dielectric function tensor in the frequency range near the phonon frequencies could be written as sum

$$\epsilon_{\alpha\beta}(\omega) = (\epsilon_\infty)_{\alpha\beta} + (\epsilon_{\text{ph}})_{\alpha\beta}(\omega) \quad (5)$$

of electronic contribution and lattice contribution, where  $\alpha, \beta = \hat{\mathbf{a}}, \hat{\mathbf{b}}, \hat{\mathbf{c}}$  are the axis indices. For  $\text{TbMn}_2\text{O}_5$ ,  $(\epsilon_\infty)_{aa}$  and  $(\epsilon_\infty)_{bb}$  were measured to be 5.31 and 6.82 respectively.<sup>10</sup> In  $\text{TbMn}_2\text{O}_5$ , the phonons are polarized along the  $a, b, c$  axis, and  $\epsilon_{\alpha\beta}(\omega)$  is diagonal. We could therefore ignore the subscripts  $\alpha, \beta$ , but only give the polarization direction. The dielectric contribution from the  $\alpha$ -polarized IR-active phonons is then

$$\epsilon_{\text{ph}}^{(\alpha)}(\omega) = \Omega_0^2 \sum_\lambda \frac{Z_\lambda^{*2}}{\omega_\lambda^2 - \omega^2}, \quad (6)$$

where  $\omega_\lambda$  and  $Z_\lambda^*$  are the mode frequencies and mode dynamical charges respectively, and  $\Omega_0^2 = 4\pi e^2/m_0 V$  is a characteristic frequency having the interpretation of a plasma frequency of a gas of objects of mass  $m_0=1$  amu, charge  $e$ , and density  $V^{-1}$  ( $V$  is the 32-atom primitive cell volume).<sup>22</sup> The sum is restricted to the  $\alpha$ -polarized phonons. The mode dynamical charges are defined as

$$Z_\lambda^* = V \frac{\partial P_\alpha}{\partial u_\lambda} \quad (7)$$

in which  $P_\alpha$  is the polarization in the  $\alpha$  direction due to a small frozen-ion amplitude of the  $\lambda$ -th phonon modes.<sup>22</sup> In practice we compute the mode dynamical charges by finite differences method following Ref. 22. Once we have the mode effective charges, we calculate the oscillator strengths of each IR-active modes  $S_\lambda = \Omega_0^2 Z_\lambda^{*2} / \omega_\lambda^2$ , and the total lattice contribution to the static ( $\omega \rightarrow 0$ ) dielectric constant  $\epsilon_{\text{ph}}(0) = \Omega_0^2 \sum_\lambda Z_\lambda^{*2} / \omega_\lambda^2 = \sum_\lambda S_\lambda$ .

The results of the Born effective charges and oscillator strengths for the IR-active modes are also listed in Table V, VI and VII, for the  $A_1$  ( $b$ -polarized),  $B_2$  ( $a$ -polarized) and  $B_1$  ( $c$ -polarized) phonons respectively.

Let us first look at the  $A_1$  ( $b$ -polarized) modes presented in Table V. There are 28  $A_1$  modes in total, and 14 (plus one acoustic mode) of them that are mainly  $B_{2u}$  IR modes. The calculated phonon frequencies and oscillator strengths are in very good agreement with experiments. The calculated total oscillator strength is about 9.24 compared with the measures value 9.12. The rest 13 modes are mainly  $A_g$  Raman modes. Under the low  $Pb2_1m$  symmetry, these modes also acquire some small oscillator strengths. More importantly, the  $693 \text{ cm}^{-1}$   $A_g$  Raman mode ( $703 \text{ cm}^{-1}$  measured from IR spectra<sup>10</sup>), that was found also IR active with oscillator strength  $S_\lambda=0.001$  in the experiment,<sup>10</sup> is well reproduced in the calculations, with oscillator strength  $S_\lambda=0.004$ , therefore, confirming that the ground state structure is indeed of  $Pb2_1m$  symmetry.<sup>16</sup> The oscillator strengths of other  $A_g$  modes might be covered by the adjacent  $B_{2u}$  modes, and therefore are not observed experimentally. To see more clearly between the coupling of the IR and Raman modes, we also list the percentage of the characters in the Table. We see the coupling between IR and Raman modes is fairly small.

The results of 28  $B_2$  phonons are given in Table VI, classified into two presentation according to their major symmetry characters, including 14 IR ( $B_{3u}$ ) modes, 13 ( $B_{1g}$ ) Raman modes and one acoustic mode. Two of the  $B_{3u}$  modes were missing in the experiments,<sup>10</sup> possibly due to their small oscillator strengths. Here we tentatively assign them as the  $465.2$  and  $509.2 \text{ cm}^{-1}$  modes. Again the phonon frequencies agree very well with the experiments. However, the IR oscillator strengths are in less agreement with the experimental values. Some modes have large discrepancy in the oscillator strengths compared to the experiments, e.g, the  $264 \text{ cm}^{-1}$  mode. Nevertheless, the calculated total oscillator strength for  $a$ -polarized phonons is about 6.87, in a reasonable agree-



TABLE VII: Calculated phonon frequencies  $\omega$ , effective charges  $Z_\lambda^*$  and oscillator strength  $S_\lambda$  of  $B_1$  modes, classified according to their major symmetry characters. The Raman-active phonons are extracted from Ref. 24.

$B_{1u}$ (IR, $c$ -polarized)				$B_{3g}$ (Raman)				
$\omega$	$Z_\lambda^*$	$S_\lambda$	Raman%	$\omega$		$Z_\lambda^*$	$S_\lambda$	IR%
GGA	GGA	GGA		GGA	Exp.	GGA	GGA	
142.2	0.49	1.65	$\sim 0$	102.6		0.005	$\sim 0$	0.004
249.5	1.01	2.27	0.62	192.1	195	0.007	$\sim 0$	0.03
300.2	0.18	0.05	3.28	241.6	244	0.100	0.024	0.41
407.4	1.47	1.828	24.58	265.5		0.040	0.003	0.69
433.9	0.84	0.53	27.42	289.0	299	0.107	0.019	1.50
495.8	1.20	0.82	36.47	325.2		0.098	0.013	1.27
527.2	0.39	0.08	2.80	426.4		2.25	3.89	48.8
605.1	0.74	0.21	0.56	447.2	442	0.116	0.009	0.45
				470.0		0.124	0.010	5.92
				505.8	540	0.909	0.450	34.5
				553.9	577	0.012	$\sim 0$	2.07

ment with the experiments value about 9.19.<sup>10</sup> Similar to the  $A_g$  modes, the  $B_{1g}$  Raman modes also have small IR oscillator strengths due to the  $Pb2_1m$  symmetry. For most modes, the coupling between the IR and Raman characters are small, except two modes: the 474  $\text{cm}^{-1}$  mode in the  $B_{3u}$  presentation and the 470 mode in the  $B_{1g}$  presentation. This is probably because they are *accidentally* degenerate in phonon frequencies, leading to large character mixing.

The phonon frequencies and oscillator strengths of the  $c$ -axis polarized  $B_1$  phonons are given in Table VII, including 8 (plus one acoustic mode)  $B_{1u}$  IR modes and 11  $B_{3g}$  Raman modes. Interestingly, there are some modes that have very large IR and Raman modes mixing in this representation. For example, the 426  $\text{cm}^{-1}$  Raman modes have about 49% IR character and very large oscillator strength of  $S_\lambda=3.89$ . However, this large Raman-IR mixing might come from that this modes accidentally degenerate with the 407 and 433  $\text{cm}^{-1}$  IR modes in the numerical calculations, and might not be the case in the real system. Unfortunately, we can not find suitable experimental IR spectra to compare with for the  $B_1$  modes. We hope future experiment can clarify this problem.

## 2. Raman spectra

The temperature-dependent Raman spectra of  $\text{HoMn}_2\text{O}_5$  and  $\text{TbMn}_2\text{O}_5$  were measured by Mihailova et al.<sup>24</sup> We compare the calculated and measured Raman spectra of  $\text{TbMn}_2\text{O}_5$  in Table VI, V, VII and VIII for the  $B_{1g}$ ,  $A_g$ ,  $B_{3g}$  and  $B_{2g}$  modes respectively. The  $A_u$  silent modes are also given in Table VIII, for they also Raman-active in structure  $L$ . Some Raman modes were missing in the experiments probably because the missing modes are of very low intensity or out of the spectral range ( $\omega < 100\text{cm}^{-1}$ ) of the experimental setup.<sup>24</sup> Once again, the calculated phonon frequencies are in very good agreement with the experimental values.

TABLE VIII: Calculated phonon frequencies  $\omega$  of  $A_2$  modes, classified according to their major symmetry characters and compared with the experimental data. The Raman-active phonons are extracted from Ref. 24.

$A_u$ (Silent)		$B_{2g}$ (Raman)		
$\omega$	Raman%	$\omega$		Raman%
GGA		GGA	Exp.	
110.2	0.04	95.9		99.9
131.4	0.09	210.6	214	99.4
226.6	6.18	231.1	232	99.9
293.9	40.7	274.2		99.4
399.4	12.6	288.9	301	60.3
425.0	3.00	337.5		99.3
497.7	5.05	441.1		89.1
529.4	1.96	448.7	455	96.9
611.5	5.65	469.6	470	92.9
		478.6	505	99.3
		562.6		99.1

So far, no IR-active modes has been observed in the Raman spectra of  $\text{TbMn}_2\text{O}_5$ . However, there is an evidence that one of the IR modes become also Raman-active in  $\text{HoMn}_2\text{O}_5$ .<sup>24</sup> Three low frequency  $A_g$  Raman modes were observed at 10 K in  $\text{HoMn}_2\text{O}_5$ ,<sup>24</sup> and they are the 217  $\text{cm}^{-1}$ , 219  $\text{cm}^{-1}$  and 226  $\text{cm}^{-1}$  modes, whereas the 219  $\text{cm}^{-1}$  mode disappears at room temperature. Since the phonons of frequencies at this range are mainly due to the vibrations of Mn and O, and less related to the  $R$  atoms, one could therefore expect there are also three Raman modes in this frequencies range for  $\text{TbMn}_2\text{O}_5$ . However, only two  $A_g$  modes (215  $\text{cm}^{-1}$  and 221  $\text{cm}^{-1}$  modes) were observed (nevertheless at  $T=300$  K) in this frequency range in  $\text{TbMn}_2\text{O}_5$ , consistent with our first-principles calculations for the  $A_g$  modes. We therefore propose that the 219  $\text{cm}^{-1}$  mode in  $\text{HoMn}_2\text{O}_5$  is actually an IR-active phonon that become also Raman-active at low temperature.



## VI. DISCUSSIONS ON THE MICROSCOPIC ORIGIN OF THE ELECTRIC POLARIZATIONS AND GIANT MAGNETOELECTRIC COUPLING

We have now firmly established that the ground state structure of  $\text{TbMn}_2\text{O}_5$  ( $L$  or  $R$ ) is indeed of symmetry  $Pb2_1m$ , allowing spontaneous polarization along the  $b$ -axis. We have calculated<sup>16</sup> the spontaneous polarization of structure  $L$  ( $R$ ) via Berry phase technique.<sup>25</sup> The *intrinsic* polarization in this material is calculated to be  $1187 \text{ nC}\cdot\text{cm}^{-2}$ .<sup>16</sup> This value is an order of magnitude smaller than that of the traditional ferroelectrics<sup>21</sup> (e.g, for  $\text{BaTiO}_3 \sim 25\mu\text{C}\cdot\text{cm}^{-2}$ ), yet it is about 30 times larger than the *currently* measured value<sup>3</sup> ( $\sim 40 \text{ nC}\cdot\text{cm}^{-2}$ ) for this compound. The reasons for the discrepancy between the calculations and experiments might be because of the approximations used in calculations. For example, we approximate the magnetic propagation vector  $k_z=0.32$  by zero. We also ignore the spin-orbit coupling and assuming collinear spins. Without these approximations, the polarization might be reduced. On the other hand, the experiment<sup>3</sup> measured polycrystalline samples, in which the grains polarize along different directions cancel each other, therefore might significantly underestimate the *intrinsic* polarization. We believe a high quality single crystal sample should greatly enhance the measured electric polarization.

To further elucidate the origin of the polarization, we calculate the spontaneous polarization for the high symmetry structure  $H$  and get  $\mathbf{P}=228 \text{ nC}\cdot\text{cm}^{-2}$ . It might be surprising to see a crystal that possesses inversion symmetry would develop spontaneous polarization at the first sight. However, to discuss the symmetry of a crystal with a magnetic ordering, the pure point groups may not be enough. One has to resort to the magnetic groups to take account of the spin components. Based on the symmetry considerations, there are three possibilities (but not exclusive) to develop spontaneous polarization:

(i) The crystal structure itself does not have inversion symmetry. This is the most familiar case to us, as it is seen in the traditional ferroelectrics.

(ii) The crystal structure itself has the  $R^{-1}$  symmetry, but the magnetic structure does not have the  $R^{-1}$  symmetry *and* the combination of the  $R^{-1}$  and time-reversal ( $T^{-1}$ ) symmetry,  $(RT)^{-1}$ . If the magnetic structure of a system does not have the  $R^{-1}$  symmetry, but still has the  $(RT)^{-1}$  symmetry, each spin channel may have finite electric polarization. However, the polarizations from spin up and spin down channels cancel each other, leading to zero total electric polarization.

(iii) Even both the crystal and magnetic structure have the inversion symmetry, but they do not have the common inversion center, as proposed by Betouras *et al.*<sup>26</sup>

In the later two cases, the “electronic” inversion symmetry is broken because of the magnetic ordering. The electronic symmetry breaking will further couple to the lattice and lead to lattice distortion. It was shown<sup>16</sup> that in  $\text{TbMn}_2\text{O}_5$ , the SC  $g$  does not have the  $R^{-1}$  and the  $(RT)^{-1}$  symmetry (case ii), because the special spin configurations of the  $\text{Mn}^{3+}\text{-Mn}^{4+}\text{-Mn}^{3+}$  chains along the  $b$  axis. Therefore, when holding atoms fixed at the centrosymmetric structure, turning on the magnetic order does two things: it generates a purely electronic polarization of  $228 \text{ nC}\cdot\text{cm}^{-2}$ , and it also applies forces to the atoms. These forces give rise to atomic displacements that yield an additional  $959 \text{ nC}\cdot\text{cm}^{-2}$ .

The above discussion is based solely on the symmetry argument. We now discuss the microscopic mechanism of coupling between the magnetic order and lattice. The microscopic origin of the ME coupling may come from<sup>8</sup>

(i) Symmetric superexchange interactions that of the *scalar* field type:  $\mathbf{S}_n \cdot \mathbf{S}_{n+1}$ .

(ii) Antisymmetric superexchange interactions that of the *vector* field type:  $\mathbf{S}_n \times \mathbf{S}_{n+1}$ .

The antisymmetric superexchange interaction (also known as Dzyaloshinskii-Moriya interaction) originate from the spin-orbit interaction. For the antisymmetric superexchange mechanism, noncollinearity is essential for the ME coupling. Experimentally, it was shown that in  $\text{TbMn}_2\text{O}_5$  the largest electric polarization is associated with a commensurate magnetic phase that is almost collinear,<sup>4,15</sup> therefore, in this phase, the spin-orbit contribution to the ME coupling is small. An alternative mechanism must be considered to account for the ME effects. In the present calculations, we ignore the spin-orbit coupling and assume collinear spin ( $\mathbf{S}_i \parallel \mathbf{S}_j$ ), therefore the symmetry breaking and ME coupling is merely due to the symmetric superexchange  $\mathbf{S}_n \cdot \mathbf{S}_{n+1}$ .

We now derive an effective model to describe the microscopic mechanism of the ME coupling in  $\text{TbMn}_2\text{O}_5$ , based on a Heisenberg model assuming NN interactions. The total energy of the system around the high-symmetry structure  $H$  can be written as,

$$E(\{u_\lambda\}) = E_0 + \frac{1}{2} \sum_{\lambda} m_{\lambda} \omega_{\lambda}^2 u_{\lambda}^2 - \sum_{ij} J_{ij}(\{u_{\lambda}\}) \mathbf{S}_i \cdot \mathbf{S}_j, \quad (8)$$

where  $u_{\lambda}$  is the  $\lambda$ -th zone-center phonon, and  $\mathbf{S}_i$  is the magnetic moment of the  $i$ -th atom. Here, we consider only the magnetic moments of the  $\text{Mn}^{3+}$  and  $\text{Mn}^{4+}$  ions.  $E_0$  is the total energy of structure  $H$  without spin-spin interactions. Since the magnetic-ordering-induced lattice distortion from structure  $H$  is small, we could expand the exchange interaction  $J_{ij}(\{u_{\lambda}\})$  up to the second order of  $u_{\lambda}$ , i.e.,

$$E(\{u_\lambda\}) = (E_0 - \sum_{ij} J_{ij}(0) \mathbf{S}_i \cdot \mathbf{S}_j) - \sum_{ij} \sum_{\lambda} \frac{\partial J_{ij}}{\partial u_\lambda} u_\lambda \mathbf{S}_i \cdot \mathbf{S}_j + \left( \frac{1}{2} \sum_{\lambda} m_\lambda \omega_\lambda^2 u_\lambda^2 - \sum_{ij} \sum_{\lambda\rho} \frac{\partial^2 J_{ij}}{\partial u_\lambda \partial u_\rho} u_\lambda u_\rho \mathbf{S}_i \cdot \mathbf{S}_j \right). \quad (9)$$

The above three terms play different roles in the multiferroics.

(i) The zeroth order term in  $u_\lambda$ ,

$$E_0 - \sum_{ij} J_{ij}(0) \mathbf{S}_i \cdot \mathbf{S}_j, \quad (10)$$

determines the ground state spin configurations which is further discussed in Appendix A.

(ii) The second term in Eq. (14) that is linear in  $u_\lambda$ ,

$$- \sum_{ij} \sum_{\lambda} \frac{\partial J_{ij}}{\partial u_\lambda} u_\lambda \mathbf{S}_i \cdot \mathbf{S}_j, \quad (11)$$

provides the driven forces for the lattice distortion from high symmetry structure  $H$ . The force on the  $\lambda$ -th phonon modes is

$$F_\lambda = - \frac{\partial E}{\partial u_\lambda} \Big|_{u_\lambda=0} = \sum_{ij} \frac{\partial J_{ij}}{\partial u_\lambda} \mathbf{S}_i \cdot \mathbf{S}_j, \quad (12)$$

which is nonzero, provided  $\{\mathbf{S}_i\}$  does not have the  $R^{-1}$  and  $(RT)^{-1}$  symmetry.

In Ref. 16, we illustrated the lattice distortion from the high symmetry structure using a spin chain model. For SC  $g$ , inside the  $\text{Mn}^{3+}\text{-Mn}^{4+}\text{-Mn}^{3+}$  segments along the  $b$ -axis,  $\text{Mn}^{4+}$  always have the same spin with the upper  $\text{Mn}^{3+}$  but opposite spin with the lower  $\text{Mn}^{3+}$ , whereas for  $g'$ , the opposite is true.  $\text{Mn}^{4+}$  could therefore move closer to the  $\text{Mn}^{3+}$  with same spin to lower the exchange energy. According to Eq. (12), we have  $F_\lambda(g) = -F_\lambda(g')$ . The high symmetry structure  $H$  then spontaneously relax to structure  $L$  or  $R$  according to its SC. The lattice distortion from high symmetry structure can be estimated as,

$$\delta u \sim \frac{\partial J}{\partial u} / \bar{\omega}^2, \quad (13)$$

where  $\bar{\omega}$  is the *weight* averaged phonon frequency. We could therefore expect that a material with larger  $\partial J / \partial u$  and softer phonon frequencies would have larger ME effects, provided the symmetry requirements are satisfied.

(iii) The quadratic term in  $u_\lambda$ ,

$$\frac{1}{2} \sum_{\lambda} m_\lambda \omega_\lambda^2 u_\lambda^2 - \sum_{ij} \sum_{\lambda\rho} \frac{\partial^2 J_{ij}}{\partial u_\lambda \partial u_\rho} u_\lambda u_\rho \mathbf{S}_i \cdot \mathbf{S}_j \quad (14)$$

describes the coupling between phonons and magnons, which renormalizes the phonon frequencies. For example, in  $\text{ZnCr}_2\text{O}_4$ ,<sup>27,28</sup> a large splitting between IR active phonons along the  $x$  and  $z$  axis was observed due

to the phonon-magnon coupling. The phonon-magnon coupling might be responsible to the “step” in dielectric constant at 24K in  $\text{TbMn}_2\text{O}_5$ . Detailed investigation of the phonon-magnon coupling in  $\text{TbMn}_2\text{O}_5$  is out of the scope of the present work, and we leave it for future investigations.

## VII. SUMMARY

We have investigated the ground state structural and electronic properties of multiferroic  $\text{TbMn}_2\text{O}_5$  using density functional theory within GGA approximations to elucidate the microscopic origin of the ferroelectricity and giant magnetoelectric coupling. We use the collinear spin approximation and ignore spin-orbit coupling. The calculated lattice and electronic structures agree well with the known experiments. We confirm that the ground state structure of  $\text{TbMn}_2\text{O}_5$  is of space group  $Pb2_1m$ , allowing polarizations. The spontaneous electric polarization is calculated to be  $1187 \text{ nC}\cdot\text{cm}^{-2}$  along the  $b$  axis. The calculated zone-center optical phonons frequencies and the oscillator strengths of IR phonons agree very well with the experimental values. Unlike the traditional ferroelectrics, no soft phonons is found in  $\text{TbMn}_2\text{O}_5$ . We derive an effective Hamiltonian to explain the magnetically-induced ferroelectricity, in which the spin-lattice coupling is of symmetric superexchange interaction type. Our results strongly suggest that the ferroelectricity in  $\text{TbMn}_2\text{O}_5$  is driven by the magnetic ordering that breaks the inversion symmetry without invoking the spin-orbit coupling.

## Acknowledgments

L.H. would like to thank D. Vanderbilt for valuable suggestions. This work was supported by the Chinese National Fundamental Research Program 2006CB921900, the Innovation funds and “Hundreds of Talents” program from Chinese Academy of Sciences.

## APPENDIX A: GROUND STATE SPIN CONFIGURATIONS

In this appendix, we discuss in more details about the magnetic structures of  $\text{TbMn}_2\text{O}_5$  and the (super)exchange interactions  $J_s$ .<sup>4</sup> To determine the  $J_s$ , we calculate the total energies of eight SCs shown in Fig.

TABLE IX: The DFT-GGA calculated total energies of spin configurations (shown in Fig. 2) under the high symmetry structure  $H$ , where  $E_3 = -2J_3 S_3 \cdot S_4$ ,  $E_4 = -2J_4 S_3 \cdot S_4$ ,  $E_5 = -2J_5 S_3 \cdot S_3$ . The exchange integrals  $J_3$ ,  $J_4$  and  $J_5$  are fitted using the total energies of four AFM structures.  $\Delta E$  are the energy differences between the fitted energies from the Heisenberg model and the calculated ones. Unit of energy is in meV, and the unit of exchange integrals are in meV/ $\mu_B^2$ .

SC	status		Energy	$\Delta E$
$a$	FM	$E_0 + 16E_3 + 16E_4 + 4E_5$	0	-179.84
$b$	FM	$E_0 - 16E_3 - 16E_4 + 4E_5$	-1355.66	-158.22
$c$	FM	$E_0 - 4E_5$	-1004.93	-8.41
$d$	FM	$E_0$	-910.32	-19.78
$e$	AFM	$E_0 + 8E_3 + 8E_4$	-596.59	0
$f$	AFM	$E_0 - 8E_3 - 8E_4$	-1263.61	0
$g$	AFM	$E_0 - 16E_4 - 4E_5$	-1624.95	0
$h$	AFM	$E_0 + 16E_4 - 4E_5$	-407.72	0
		$J_3 = -0.45$ $J_4 = -4.92$ $J_5 = -1.85$		

2, under the fixed *high* symmetry structure  $H$ . The total energies of these SCs are listed in Table IX, among which SC  $g$  has the lowest total energy. We then use a Heisenberg model with NN interaction,

$$E = E_0 - \sum_{ij} J_{ij} \mathbf{S}_i \cdot \mathbf{S}_j, \quad (\text{A1})$$

to fit  $J$ s and to check whether the  $g$  is indeed the ground state SC. Here,  $\mathbf{S}_i$  is the spin of the  $i$ -th Mn ion and  $J_{ij}$  denotes the exchange integral between two NN  $i$ -th and  $j$ -th atoms.  $J_3$ ,  $J_4$  and  $J_5$  are fitted using four AFM SCs, and the results are listed in Table IX. Since  $J_1$  and  $J_2$  is not relevant here, they are not fitted. We calculate the total energies of the four FM SCs from Eq.(A1). These results are in reasonable good agreement

with the first-principles calculations, suggesting that the Heisenberg model is valid even in the FM phase when applied to  $\text{TbMn}_2\text{O}_5$ . From Table IX, we find all the three exchange integrals are negative, i.e., of AFM type, and  $|J_3| \ll |J_4|, |J_5|$ . Therefore the ground state SC are mainly determined by  $J_4$  and  $J_5$ . It is easy to see that SC  $g$  (and  $g'$ ) indeed has the lowest energy in this model.

In both SCs  $g$  and  $g'$ ,  $\text{Mn}^{4+}$  form an AFM square lattice in the  $ab$  plane, whereas  $\text{Mn}^{3+}$  couples to  $\text{Mn}^{4+}$  either antiferromagnetically via  $J_4$  along the  $a$  axis or with alternating sign via  $J_3$  along the  $b$  axis. The zigzag chains along the  $b$  axis can be simplified as  $\text{Mn}^{3+}$ - $\text{Mn}^{4+}$ - $\text{Mn}^{3+}$  segments linked via  $J_5$  superexchange interactions. Inside the segments  $\text{Mn}^{3+}$  and  $\text{Mn}^{4+}$  interact through superexchange  $J_3$ , whereas the chains couple to each other through  $J_4$ . The AFM chains along the  $a$  axis are of two types, labeled as I and II respectively in Fig. 3. Adjacent chains I and II along the  $b$  axis couple to each other via  $J_3$ , in which half of them are frustrated.

The SCs  $g$  and  $g'$  have several energetically degenerate SCs as shown in Fig. 3. There are two relative positions between chain I and II,  $l$  and  $r$ . “ $l$ ” (“ $r$ ”) means that the  $\text{Mn}^{4+}$  ions in chain I have the same spins to the  $\text{Mn}^{4+}$  ions on their *left* (*right*) side in chain II in each unit cell. Figure 3 shows 4 different combinations of chains I and II. Figure 3(a) and (b) are the ground SC  $g$  and  $g'$  respectively, whereas Fig.3(c) and (d) are in fact two domain wall structures  $dw$  and  $dw'$ . The two domain walls are energetically degenerate to  $g$  and  $g'$  in the NN Heisenberg model, because the  $J_3$  exchange interactions between chain I and II cancel out no matter what their relative positions are. However, after turning on the spin-lattice coupling, the crystal structure  $H$  will relax to  $L$  or  $R$ , and the energy degeneracy between the domain wall structures ( $dw$  and  $dw'$ ) to SCs  $g$  and  $g'$  will be lifted.

<sup>1</sup> T. Kimura, T. Goto, H. Shintani, K. Ishizaka, T. Arima, and Y. Tokura, *Nature*(London) **426**, 55 (2003).  
<sup>2</sup> T. Goto, T. Kimura, G. Lawes, A. P. Ramirez, and Y. Tokura, *Phys. Rev. Lett.* **92**, 257201 (2004).  
<sup>3</sup> N. Hur, S. Park, P. A. Sharma, J. S. Ahn, S. Guha, and S.-W. Cheong, *Nature* (London) **429**, 392 (2004).  
<sup>4</sup> L. C. Chapon, G. R. Blake, M. J. Gutmann, S. Park, N. Hur, P. G. Radaelli, and S. W. Cheong, *Phys. Rev. Lett.* **93**, 177402 (2004).  
<sup>5</sup> G. R. Blake, L. C. Chapon, P. G. Radaelli, S. Park, N. Hur, S.-W. Cheong, and J. Rodriguez-Carvajal, *Phys. Rev. B* **71**, 214402 (2005).  
<sup>6</sup> N. Hur, S. Park, P. A. Sharma, S. Guha, and S.-W. Cheong, *Phys. Rev. Lett.* **93**, 107207 (2004).  
<sup>7</sup> S.-W. Cheong and M. Mostovoy, *Nature Materials* **6**, 13 (2007).  
<sup>8</sup> M. Fiebig, *J. Phys. D: Appl. Phys.* **286**, R123 (2005).  
<sup>9</sup> I. Kagomiya, S. Matsumoto, K. Kohn, Y. Fukuda, T. Shoubu, H. Kimura, Y. Noda, and N. Ikeda, *Ferroelectrics* **286**, 889 (2003).

<sup>10</sup> R. ValdesAguilar, A. B. Sushkov, S. Park, S. W. Cheong, and H. D. Drew, *Phys. Rev. B* **74**, 184404 (2006).  
<sup>11</sup> H. Katsura, N. Nagaosa, and A. V. Balatsky, *Phys. Rev. Lett.* **95**, 057205 (2005).  
<sup>12</sup> I. A. Sergienko and E. Dagotto, *Phys. Rev. B* **73**, 094434 (2006).  
<sup>13</sup> J. A. Alonso, M. T. Casais, M. J. Martinez-Lope, J. L. Martinez, and M. T. Fernandez-Diaz, *J. Phys.: Condens. Matter* **9**, 8515 (1997).  
<sup>14</sup> J. Hu, arXiv:0705.0955.  
<sup>15</sup> L. C. Chapon, P. G. Radaelli, G. R. Blake, S. Park, and S.-W. Cheong, *Phys. Rev. Lett.* **96**, 097601 (2006).  
<sup>16</sup> C. Wang, G.-C. Guo, and L. He, *Phys. Rev. Lett.* (2007).  
<sup>17</sup> J. P. Perdew, K. Burke, and M. Ernzerhof, *Phys. Rev. Lett.* **77**, 3865 (1996).  
<sup>18</sup> G. Kresse and J. Hafner, *Phys. Rev. B* **47**, RC558 (1993).  
<sup>19</sup> G. Kresse and J. Furthmuller, *Phys. Rev. B* **54**, 11169 (1996).  
<sup>20</sup> P. E. Blochl, *Phys. Rev. B* **50**, 17953 (1994).  
<sup>21</sup> M. E. Lines and A. M. Glass, *Principles and Applications*

- of Ferroelectrics and Related Materials* (Oxford University Press, 2001).
- <sup>22</sup> L. He, J. B. Neaton, M. H. Cohen, D. Vanderbilt, and C. C. Homes, Phys. Rev. B **65**, 214112 (2002).
  - <sup>23</sup> H. T. Stokes and D. M. Hatch, SMODES, [www.physics.byu.edu/stokesh/isotropy.html](http://www.physics.byu.edu/stokesh/isotropy.html). (1999).
  - <sup>24</sup> B. Mihailova, M. M. Gospodinov, B. Guttler, F. Yen, A. P. Litvinchuk, and M. N. Iliev, Phys. Rev. B **71**, 172301 (2005).
  - <sup>25</sup> R. D. King-Smith and D. Vanderbilt, Phys. Rev. B **47**, 1651 (1993).
  - <sup>26</sup> J. J. Betouras, G. Giovannetti, and J. van den Brink, Phys. Rev. Lett. (2007).
  - <sup>27</sup> A. B. Sushkov, O. Tchernyshyov, W. Ratcliff, S. W. Cheong, and H. D. Drew, Phys. Rev. Lett. **94**, 137202 (2005).
  - <sup>28</sup> C. J. Fennie and K. M. Rabe, Phys. Rev. Lett. **96**, 205505 (2006).